JOURNAL OF SPACECRAFT AND ROCKETS
Vol. 36, No. 2, March–April 1999

Computational Aeroheating Predictions for X-34

William L. Kleb,[*] William A. Wood,[*] and Peter A. Gnoffo[†]
NASA Langley Research Center, Hampton, Virginia 23681
and
Stephen J. Alter[‡]
Lockheed Engineering and Sciences Company, Hampton, Virginia 23681

Radiative equilibrium surface temperatures, heating rates, streamlines, surface pressures, and flowfield features as predicted by the LAURA are presented for the X-34 Technology Demonstrator. Results for two trajectory points corresponding to entry peak heating and two control-surface deflections are discussed in detail, outlining the effects of the boundary-layer state and various flow features on the heat transfer rates and corresponding wall temperatures. These data are also discussed in the context of thermal protection system design issues, indicating that only minor changes needed to be made to the existing layout. The work presented is part of a larger effort to define the X-34 aerothermal environment, including the application of engineering codes and wind-tunnel studies.

Nomenclature

b = wingspan, 27.7 ft
H = ratio of local heat-transfer coefficient and stagnation point heat-transfer coefficient
h = altitude, kft
L = overall vehicle length, 58.3 ft
L' = overall vehicle length w/o body flap
M = Mach number
$\bar{p}$ = pressure nondimensionalized by freestream density and the square of the freestream velocity
q = heating rate, Btu/ft^2-s
Re = Reynolds number
T = temperature, °F
V = velocity, ft/s
x = fuselage station, ft
y = buttline station, ft
z = waterline station, ft
α = angle of attack, deg
δ_{cs} = control-surface deflections, deg (+down)
ϵ = emissivity
ρ = density, slug/ft^3
σ = Stefan–Boltzmann constant, 4.76×10^{-13} Btu/ft^{2}R^4-s

Subscript

∞ = freestream conditions

Introduction

As early as May 1993, Orbital Sciences Corporation (OSC) of Dulles, Virginia, began considering low-cost methods to launch relatively small payloads (~1500 lb) into space.[1,2] In the fall of 1993, OSC approached NASA to inquire about an alliance that would utilize the Agency's space transportation knowledge base, facilities, and analysis tools. Subsequently, Presidential Decision Directive NSTC-4 led NASA to announce a Cooperative Agreement Notice[3] to build a small reusable launch vehicle (RLV) designated X-34.[1,2,4–6] This was awarded to OSC, teamed with Rockwell International, in the Spring of 1995. By February 1996, however, OSC and Rockwell had determined that the venture would not be profitable and withdrew from the agreement.[7,8] In the spring of 1996, NASA solicited proposals for a different vehicle, also designated X-34. OSC was awarded this contract in June of 1996.

The new X-34 is to be a suborbital technology demonstrator, capable of flying to Mach 8, reaching an altitude of 250,000 ft, and landing autonomously on a conventional runway. A typical mission profile is shown in Fig. 1. The vehicle is launched from OSC's L-1011, ignites its liquid rocket engine, ascends to altitude, and then coasts to a down-range landing—a very similar mission profile to the X-15 nearly 40 years previous.[9] The vehicle is to serve as a testbed for a multitude of RLV technologies such as composite airframe and propellant tank components, low-cost avionics via the Global Positioning System, and a flush air data system.[10,11]

This paper presents results used to define and design the thermal protection system (TPS) necessary for the vehicle's entry into the Earth's atmosphere. This work is part of a larger effort used to design the TPS, including engineering codes, arc-jet facilities, and wind-tunnel studies.[12–16] The TPS is predominately insulation blankets of the flexible reusable surface insulation (FRSI) class with silicone impregnated reusable ceramic ablator (SIRCA) tiles[16] used only on the leading edges.

NASA Langley Research Center's aerothermal contributions consisted of several focused efforts. This paper describes three benchmark-quality, full-vehicle, flight condition computations using state-of-the-art computational fluid dynamics (CFD) to ascertain TPS split lines according to material temperature limits. (An additional case that does not include the aft portion of the vehicle is also presented.) Riley et al.,[12] anchored to these results, expanded the trajectory envelope using a coupled, inviscid boundary-layer method. Incorporating the data from this limited array of trajectory points, Wurster et al.[14] developed a time history of heating rates for the entire trajectory using engineering codes. This analysis yields the heat load for over 60 points on the vehicle, providing data necessary to determine the appropriate TPS thickness. In addition to the preceding, Berry et al.[13] created an extensive database with several wind-tunnel entries, investigating effects of Mach number, configuration, angle of attack, Reynolds number, and control-surface deflections.

The remainder of this paper begins with a discussion of the numerical tool and geometry employed and is followed by a brief discussion of the trajectory and the selected points. Next are the results, consisting of a detailed description of the dominant flow features, comparisons with experiment, surface shear patterns, surface

---

Presented as Paper 98-0879 at the AIAA 36th Aerospace Sciences Meeting, Reno, NV, Jan. 12–15, 1998; received Feb. 13, 1998; revision received Sept. 18, 1998; accepted for publication Oct. 1, 1998.

[*] Research Engineer, Aerothermodynamics Branch, Aero- and Gas-Dynamics Division, Research and Technology Group.

[†] Senior Research Engineer, Aerothermodynamics Branch, Aero- and Gas-Dynamics Division, Research and Technology Group. Associate Fellow AIAA.

[‡] Senior Aeronautical Engineer. Senior Member AIAA.

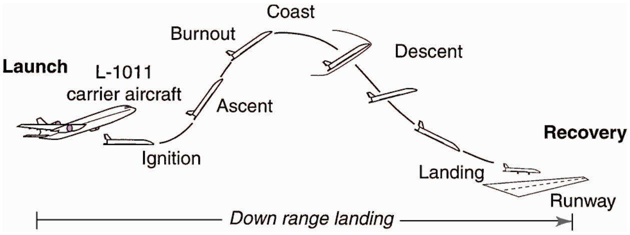

Fig. 1 Typical X-34 mission profile.

temperatures, heating rates, and pressures. Finally, a discussion of TPS design issues are discussed, followed by concluding remarks.

Numerical Method

In the hypersonic continuum regime the LAURA CFD tool[17,18] is used to describe the aerothermodynamics of X-34. LAURA is an upwind-biased, point-implicit relaxation algorithm for obtaining the numerical solution to the Reynolds-averaged Navier–Stokes equations for three-dimensional viscous hypersonic flows in thermochemical nonequilibrium.[19] The upwind-biased inviscid flux is constructed using Roe's flux-difference-splitting[20] and Harten's entropy fix[21] with second-order corrections based on Yee's symmetric total-variation-diminishing scheme.[22] LAURA is the same computational tool that has been used to describe the aerothermodynamics of blunt body shapes such as Mars Pathfinder,[23,24] Mars Microprobe,[25] Stardust,[26] and COMET,[27] and other vehicles such as X-33 (Ref. 28), HL-20 (Ref. 29), Space Shuttle,[30–32] and Reentry-F.[33]

For all of the results contained within, LAURA was run assuming air to behave as a perfect gas, and the full Navier–Stokes equations were slightly simplified via the thin-layer assumption (see Ref. 34 for rationale). Furthermore, for nearly all of the results presented, the flow was assumed to be fully turbulent because of the early transition expected for suborbital flights. Turbulence was modeled via the Baldwin–Lomax algebraic model[34] modified with a damping term according to Gupta et al.,[35] implemented by Cheatwood.[36] However, selected laminar results also are presented to bound the problem. A higher-order turbulence model, e.g., Spalart–Allmaras[37] or a two-equation model, which may be more appropriate for the massively separated flow on the lee side of the vehicle, was not available in LAURA at the time of this study.

The wall-temperature boundary condition is specified as the radiation-equilibrium, wall temperature according to the Stefan–Boltzmann relation

$$q = \sigma \epsilon T^4 \tag{1}$$

The radiative-equilibrium wall temperature T is coupled during the solution procedure with the wall heating rate q where ϵ is the surface emissivity and σ is the Stefan–Boltzmann constant. For this study a constant emissivity of 0.8 was used for all surfaces.

This coupled solution procedure between wall temperature and wall heating rate yields accurate temperature and heating rates because of the good insulation features of the selected TPS blankets.

Geometry

The X-34 geometrical description used in this study is designated X0001215 as received from OSC in Initial Graphics Exchange Specification format.[38] Figure 2 shows the X-34 geometry as modeled. Overall, the vehicle is similar to the Space Shuttle, having a cranked delta-wing planform and vertical tail. Note, however, that the fuselage transitions to rectangular cross section approximately midway back and that the wing terminates before reaching the aft end of the vehicle. The vehicle's gross takeoff weight is 45,000 lb and has a 27.7-ft wingspan b with an overall length L of 58.3 ft.

The coordinate axes are defined in the typical body-oriented manner: x running longitudinally, y along the starboard wing, and z defined by the right-hand rule, pointing upward with the origin located at the nose. Note that OSC uses a different origin location.

Small modifications were made to the original geometry to allow more tractable grid generation and facilitate obtaining the CFD solutions. These modifications consisted of the following:

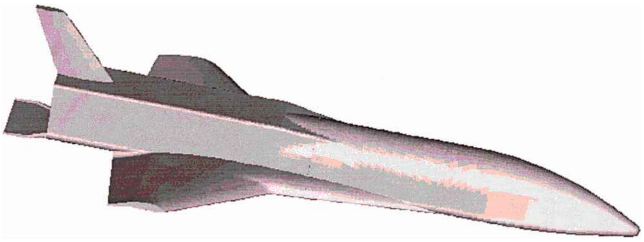

a) Lee-side view

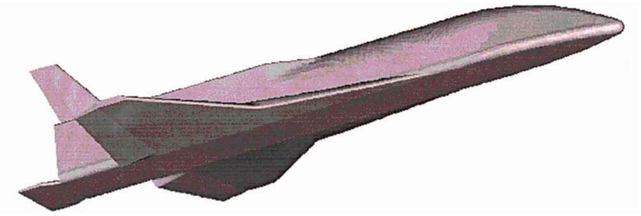

b) Wind-side view

Fig. 2 X-34 geometry.

1) Backward- or forward-facing steps created by TPS material interfaces such as that caused by the wing leading-edge SIRCA tiles and the low heat blankets (LHB) were not preserved as sharp steps. The surface grid lines were mapped onto the stepped surface, but no attempt was made to align them with the discontinuities. As a result, the sharp steps are replaced by ramps.

2) The span-wise gaps between the elevons and the body and the elevons and the ailerons were filled in. Any other gaps or surface irregularities have not been modeled. Past experience has shown that when elevons and ailerons are slaved to move together, as is the case for the hypersonic portion of the X-34's flight profile, the effects of the gap between them is a highly localized phenomenon as shown by Berry et al.[13] However, filling the gap between the body and the elevon has a larger effect on the overall flowfield because it channels flow that would normally have passed through to the lee side onto the aft portion of the vehicle's empenage.

3) The lower, aft portion of the tail surface overhanging the back of the vehicle was clipped off to provide a continuous supersonic outflow boundary condition.

4) The vehicle wake and base region including the engine nozzle and lee side of the body flap were neither modeled nor computed.

The surface and volume meshes were generated using the Integrated Computer-Aided Engineering and Manufacturing System for CFD,[39] GRIDTOOL,[40] GRIDGEN,[41] the Three-Dimensional Multiblock Advanced Grid Generation System (3DMAGGS),[42] and the Volume Grid Manipulation code (VGM)[43] as described by Alter.[44] Grid convergence studies were not performed specifically for this vehicle or case, but grid parameters were set based on past experience with heating-rate comparisons in similar situations.[23–33] Typically 64 cells were used normal to the body with stretching rates below 1.15 and wall-cell Reynolds numbers based on the speed of sound on the order of 10. In addition, each flowfield grid is adapted to the bow-shock structure to maximize efficiency. A typical full-vehicle grid including the body flap and wing wake has a total of 70 blocks and 9×10^6 grid points (see Ref. 44 for more details).

Trajectory Cases

Figure 3 shows stagnation-point heating rates for a 7.11-in. radius sphere, the nose radius of the X0001215 configuration, as predicted by Fay and Riddell theory for three different X-34 trajectories provided by OSC. The X1004701 trajectory was used by Palmer et al.[15] and Milos et al.[16] to predict the heating environment to be encountered by the nose cap and wing leading-edge SIRCA tiles. The X1004601 trajectory was used as the reference heating trajectory for the overall TPS design per OSC's request. The actual flight trajectory is anticipated to be closer to X1003904.

Table 1 presents the freestream conditions and control-surface deflections for the cases computed. (For case 2b the solution was

Table 1 Freestream conditions and control-surface deflections

Case	δ_{cs}, deg	h, kft	M_∞, (−)	α, deg	V_∞, ft/s	ρ_∞, slug/ft^3	T_∞, °F	Re_L, (−)
1a	0	118.4	6.3	23	6490	1.42×10^{-5}	−22	16×10^6
1b	10	118.4	6.3	23	6490	1.42×10^{-5}	−22	16×10^6
2a	0	112.1	6	15.2	6110	1.89×10^{-5}	−30	21×10^6
2b	10	112.1	6	15.2	6110	1.89×10^{-5}	−30	21×10^6

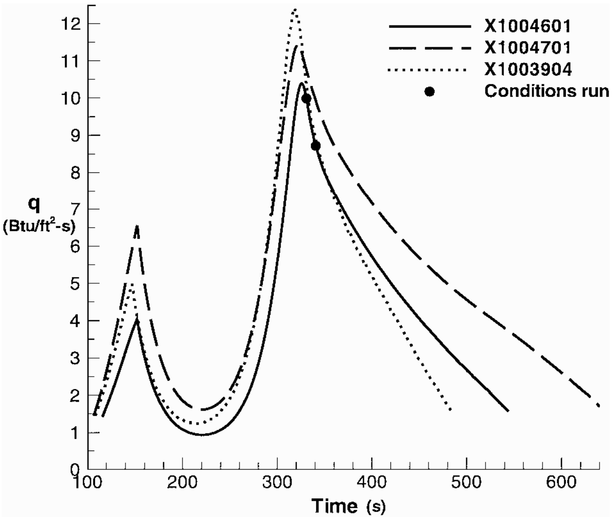

Fig. 3 Stagnation-point heating for three X-34 trajectories.

not computed aft of the wing trailing edge.) The two points shown in Table 1 are taken from the X1004601 trajectory and correspond to peak nose-cap heating and slightly thereafter when the angle of attack is significantly lowered.

Results

First, the dominant flowfield features are presented and analyzed to provide a basis for the discussion of the results to follow. Next, a comparison with experimental data of Berry et al.[13] is given in the form of near-surface streamlines via the oil-flow technique and surface heat-transfer rates via the phosphor thermography technique.[45] Surface distributions of temperature are presented next, followed by a sample of the associated heating rates and an example of the effects of a laminar or turbulent boundary layer.

The results presented here are a subset of the data produced during this study; the full data set is available in Ref. 46, which also provides enlarged figures, making some of the described features easier to discern. (Discontinuities in the figures are a result of block-to-block averaging errors when a block-marching solution strategy was used. These discontinuities are aesthetic only; the computational cell-centered values are globally conservative and consistent across block-to-block boundaries.)

Dominant Flowfield Features

Figure 4 shows three stream-wise cuts for case 1b with contours of pressure $\bar{p}$, which has been nondimensionalized by freestream density and the square of freestream velocity. Figure 4a also includes red lines indicating the location of the other two stream-wise cuts and, in blue, the locations of span-wise cuts that are shown in Figs. 5 and 6.

As shown in Fig. 4a, the forebody of the vehicle is enveloped in a highly swept bow shock that intersects with the wing-induced shock. As the flow passes the wing tip, the outer wing shock sweeps aftward because of the expansion.

Figure 4b depicts a stream-wise cut along the fuselage outboard of the centerline. The wind-side bow shock is shown clearly. Also shown are the faint remnants of the shock created by the deflected elevons, and, at the aft end of the vehicle, the embedded shock from the deflected body flap. The lee-side shock is also apparent, although somewhat smeared because of a highly stretched grid in this region.

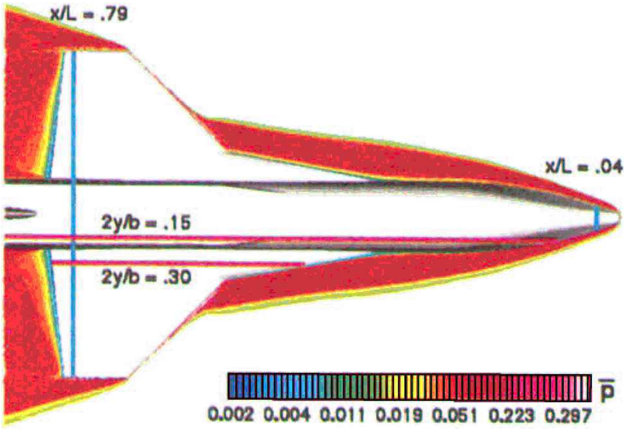

a) In the plane of wing leading edge and nose cap

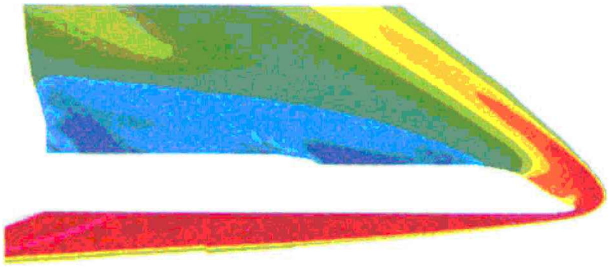

b) Vertically, along fuselage ($2y/b = 0.15$)

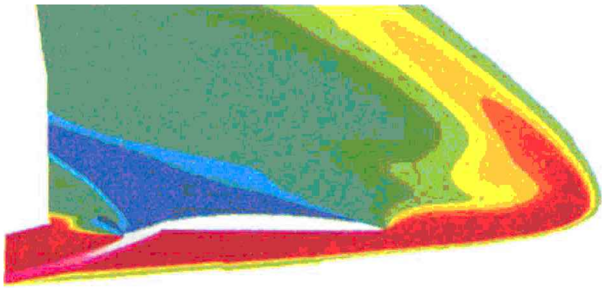

c) Vertically, along wing and strake ($2y/b = 0.30$)

Fig. 4 Nondimensional pressure contours for various stream-wise cutting planes (case 1b).

Toward the front, on the lee side, a small expansion-recompression is evident because of a TPS transition. This expansion-recompression is followed by a rapid expansion over the canopy region. A second, slight compression is also noticeable because of cross-flow effects from the side of the fuselage. This compression is followed by further expansion until the point where the fuselage transitions from a rounded cross-sectional shape to one with a considerably smaller corner radius (see Fig. 2a). At this juncture a shock is generated, which is then followed by a small expansion when the transition is complete. The wake of the wing is responsible for the area of lowest pressure just ahead of the tail, which again raises the pressure slightly because of an embedded shock.

Figure 4c shows a stream-wise cut further away from the centerline, but still well inside of the bow-shock/wing-shock interaction. The shock generated by the deflected control surface is readily apparent on the wind side. Another dominant feature present is the wake of the wing and strake, which is altered by a fish-tail shock structure emanating from the trailing edge of the wing.

Span-wise cuts for case 1b are shown in Figs. 5 and 6. (Recall that the relative vehicle locations are depicted by the blue lines in Fig. 4a.) Figure 5 shows cross-flow streamlines colored by pressure, and Fig. 6 shows Mach number contours from 0.2 to 9.0 in increments of 0.2. No explicit scale is given, and, as with Fig. 4, blue indicates low pressures whereas red indicates high pressures.

Figures 5a and 6a are taken on the forebody just behind the nose cap. A pair of wind-side vortices is clearly seen near the centerline.

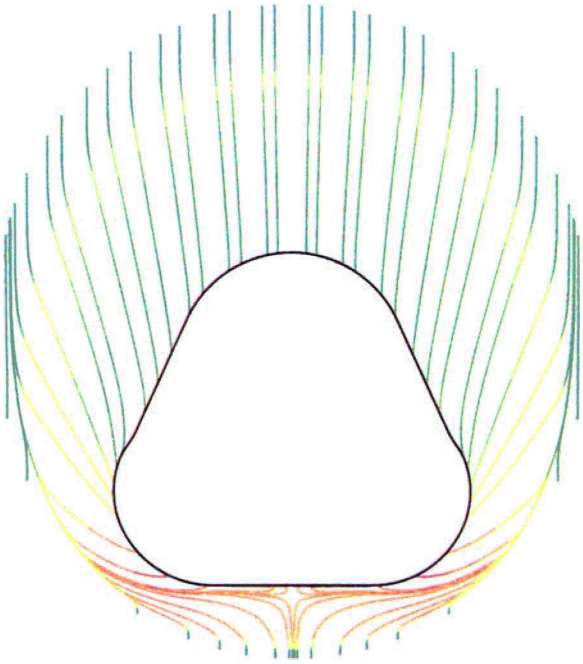

a) Downstream of spherical nose cap ($x/L = 0.04$)

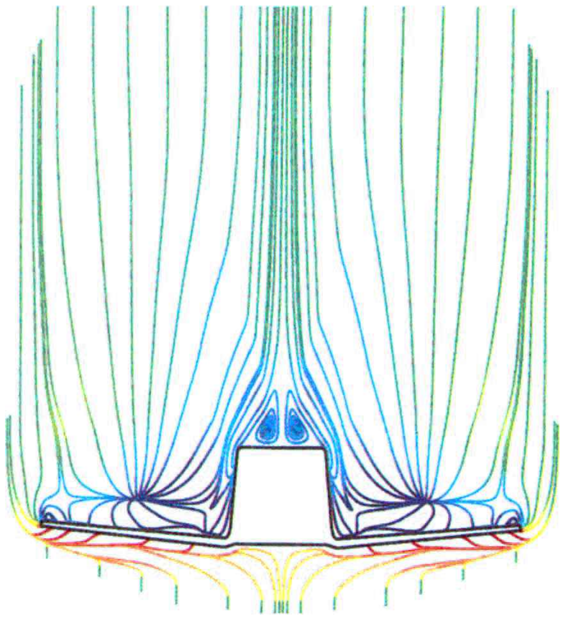

b) Before wing trailing edge ($x/L = 0.79$)

Fig. 5 Crossflow streamlines colored by pressure (case 1b).

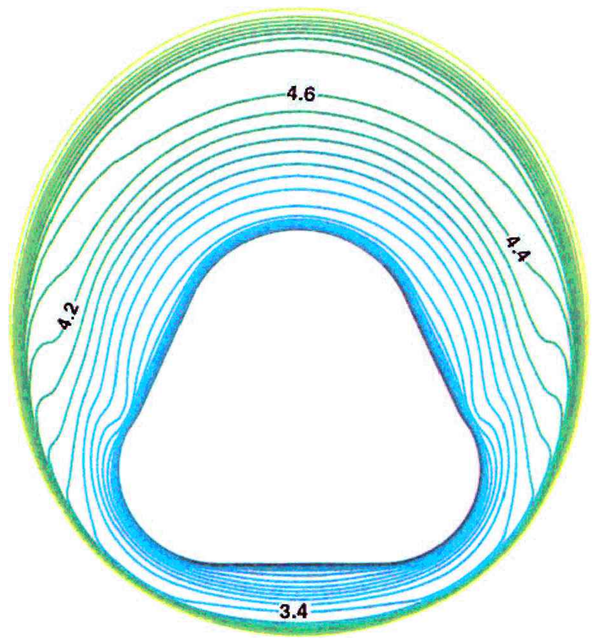

a) Downstream of spherical nose cap ($x/L = 0.04$)

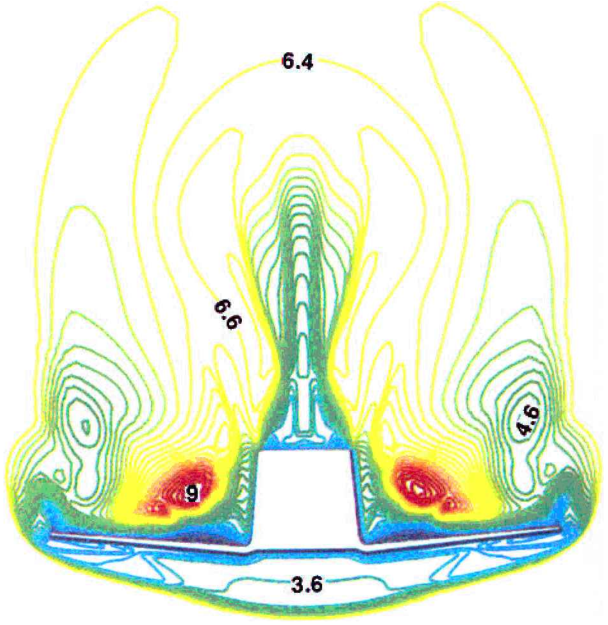

b) Before wing trailing edge ($x/L = 0.79$)

Fig. 6 Mach contours, $\Delta M = 0.2$ (case 1b).

There is no evidence of vortices on the lee side at this axial station. The overexpansion and subsequent compression is evident along the side of the fuselage.

A very different picture is evident in Fig. 5b, which shows a cross section located near the wing trailing edge. There is no longer any evidence of the wind-side vortices, and a pair of well-defined vortices sit on the lee side of the fuselage. Small wing-tip vortices are present, and the wing-strake vortices lie along the side of the fuselage. The source structure above the wing at midspan is merely the demarcation of inboard/outboard span-wise flow as well as the location where the flow has either a positive or negative vertical component. Also apparent is a small separation bubble on the inboard wing lee side.

On the wind side the embedded shock due to the deflected control surface is also clearly indicated by a merging of streamlines paralleling the deflected control surfaces. Figure 6b also shows the presence of the extensive hour-glass-shaped cross-flow shock standing on the fuselage. This shock serves to turn the flow parallel to the vehicle symmetry plane. The vertical gradients in Mach number between the cross-flow shocks (which are not present in pressure; see Fig. 5b) are believed to mark the entropy interface between flow that has gone through only the bow shock and that which has gone through both the bow and cross-flow shocks.

Next, the flowfield in the vicinity of the body flap is examined with Figs. 7 and 8. Looking from the underside of vehicle, Fig. 7 shows the view in the vicinity of the body-flap notch region. The vehicle extends off to the right, and the rest of the body flap continues to the left. The back surface of the vehicle is truncated because of the limited computational domain used to model this region. Near-surface streamlines are shown colored by pressure variation. A stream-wise stagnation line is clearly evident along the leading edge of the body-flap notch; this is created by the flow expanding around the bottom, aft corner of the vehicle. In fact, as shown by the series of span-wise cross-sectional cuts of density contours in Fig. 8, the flow is strong enough to create an embedded shock along the leading edge of the body-flap notch. The viewpoint is from the

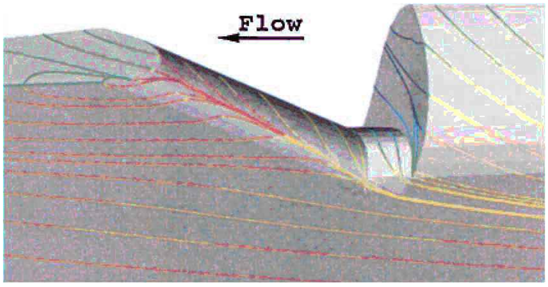

Fig. 7 Streamlines colored by pressure in the vicinity of the body-flap notch viewed from the wind side (case 1a).

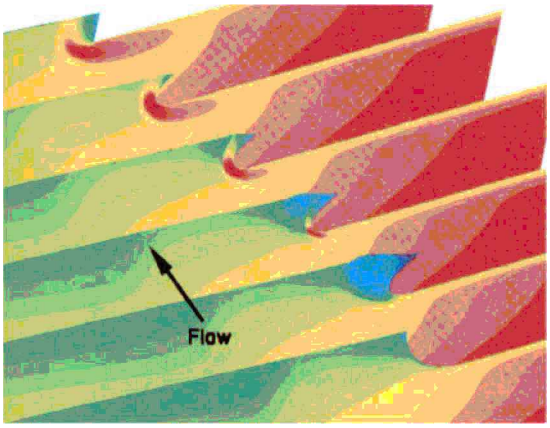

Fig. 8 Span-wise cross-sectional cuts showing density contours along the aft of the vehicle and the body flap (case 1a).

top of the wing, looking aft toward the side of the body flap (the body and body-flap surfaces have been removed). The first cross section contains the aft end of the vehicle, with the following cross sections in the notched area, and the last cross section just after the body flap regains its full span.

Because the grid topology in the notch region was such that it was not possible to run the notch block with the algebraic turbulence model as implemented, this block was run using the laminar Navier–Stokes equations. As a consequence, any surface wetted by flow emanating from the notch region has erroneous surface temperatures. However, from investigations comparing the purely laminar results and the mixed turbulent-laminar results, the basic flow structure in this area remains unaffected. This lack of influence on the basic flow structure is fortunate because Fig. 7 shows that there is a dividing streamline between the flow that remains on the wind side and the flow that travels onto the side wall and then returns to the wind side; this serves to limit the contamination caused by the embedded laminar block.

Comparison with Experiment

Surface Shear Patterns

Computer-simulated near-surface streamlines at flight conditions are shown in Fig. 9 for case 2a, assuming a turbulent boundary layer. Note that the streamlines shown in the planform views are not symmetric because of asymmetric seed points and not because of flow asymmetry. Figure 10 shows the corresponding oil flow from a Mach 6 wind-tunnel run where the attached flow over model is assumed to be transitional or turbulent.[13] Note in the windward image (Fig. 10a) that the small circular regions in the vicinity of the control-surface gaps are artifacts of oil that sags (due to gravity) prior to acquisition of these postrun photographs.

Comparing wind-side flow features, both data sets show similar indications of wind-side vortex patterns (refer to Fig. 5a) scrubbing the boundary layer toward the centerline on the forward quarter of the vehicle. Forced by a span-wise pressure gradient generated by

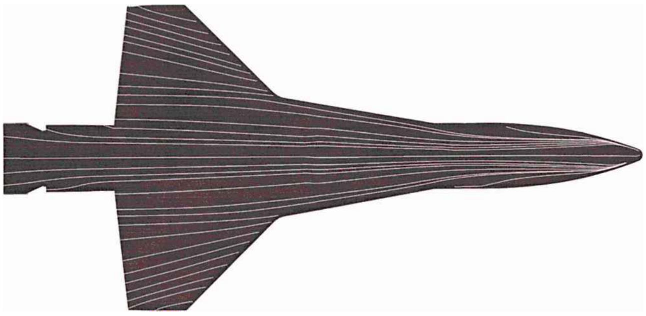

a) Wind side

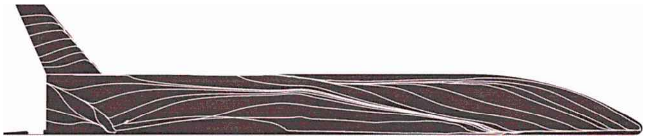

b) Starboard side

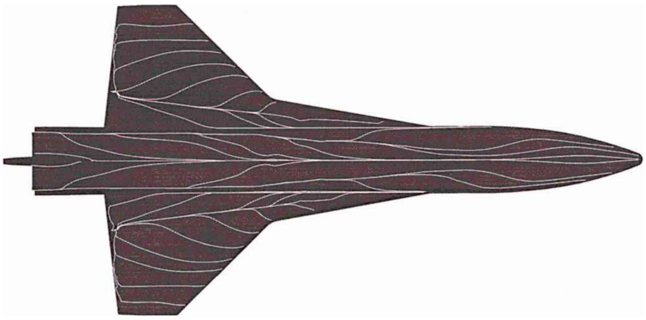

c) Lee side

Fig. 9 Computed near-surface streamlines (case 2a).

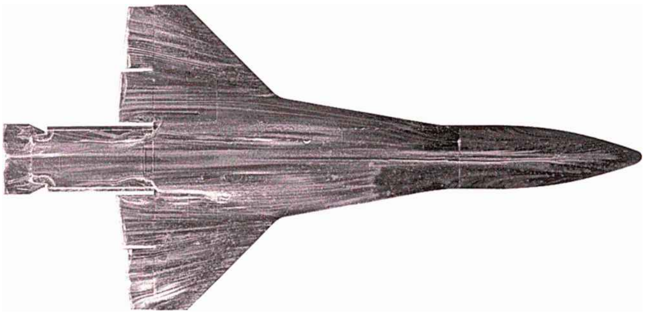

a) Wind side

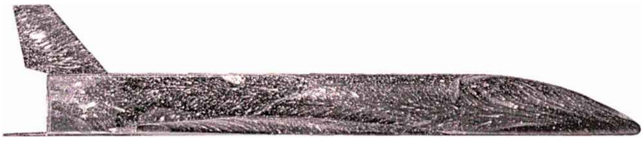

b) Starboard side

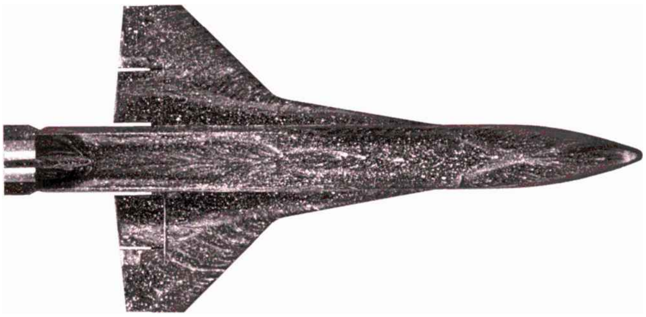

c) Lee side

Fig. 10 Oil flow for Mach 6 conditions from Ref. 13 (α = 15 deg, δ_{cs} = 0 deg, and Re_L = 4.65 × 10^6).

the nose geometry, which transitions from a spherical cross section to a rounded, triangular shape, the wind-side flow is initially converging toward the centerline. After a quarter of the vehicle, the centerline boundary layer has thickened, and these wind-side vortices dissipate, establishing the streamline patterns containing an outboard component that dominates the surface flow over the latter three-fourths of the vehicle. The surface discontinuity at the wing-fuselage junction gives rise to a slight change in the streamline patterns, more visible in the experimental results. Both data sets show a divergence of streamlines emanating from the wing-strake joint, which is next to the bow-shock impingement region.

Side-view comparisons show very good agreement, particularly in the forebody patterns. Both data sets show a strong cross-flow shock location and the separation line on the fuselage caused by the vortex emanating from the strake. A strong interaction region is seen, particularly in the computational solution, on the fuselage aft of the wing trailing edge. There is a bleed-through effect in this region on the experimental model because of the elevon gap, which is not modeled in the numerical simulation.

Lee-side surface features are in good agreement between the data sets, showing the strong cross-flow shock separation on the fuselage and the strake vortex across the wing, close to the fuselage. Inboard flow is seen over much of the wing while the fuselage shows outboard flow, generated by a longitudinal recirculation zone. Turning and separation, with a probable horseshoe vortex, occurs in front of the vertical tail.

Heat-Transfer Rates

This section provides further comparison with the experimental data of Berry et al.[13] in the form of a nondimensional heat-transfer coefficient H. Experimentally, the heat-transfer coefficients are obtained using the phosphor thermography technique discussed in Ref. 45. For the purpose of these comparisons, LAURA was run for wind-tunnel conditions of Mach 6, 15-deg angle of attack, and a Reynolds number of 8×10^6 (Ref. 47).

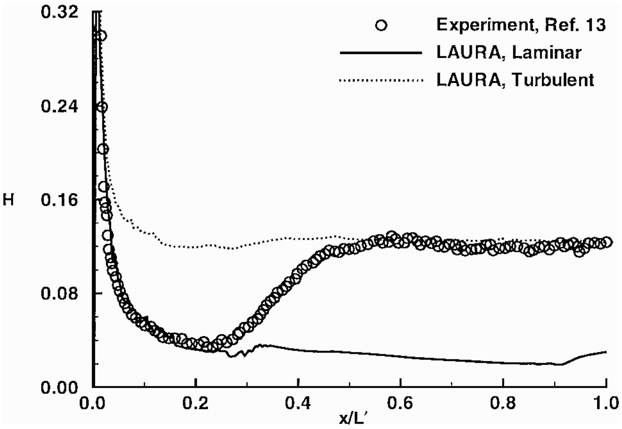

a) $2y/b = 0.0$ (centerline)

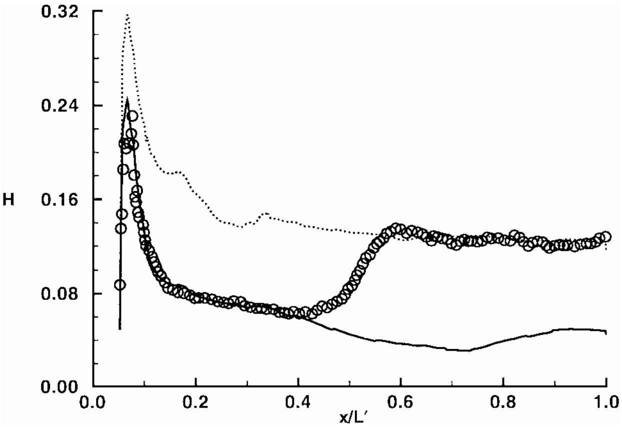

b) $2y/b = 0.1$

Fig. 11 Comparison of wind-side heat transfer measured by the phosphor thermography technique[45] and that computed by LAURA for two longitudinal cuts (Mach 6, α = 15 deg, $Re_L = 8 \times 10^6$, and δ_{cs} = 0 deg).

Figure 11 shows two wind-side longitudinal-cut comparisons of experimental and computed heat transfer. Figure 11a shows the wind-side centerline, whereas Fig. 11b shows a station 10% outboard. The experimental data contain natural transition from laminar to turbulent flow along the vehicle. Consequently, both the fully laminar and the fully turbulent LAURA results are shown. When comparing the appropriate computational data (either laminar or turbulent) with that from experiment, the agreement is within 5%. Note that even when the flow is modeled as fully turbulent, the heat-transfer levels on the rear of the vehicle are still predicted accurately even though the experiment indicates laminar flow on the forebody.

Figure 12 shows global wind-side comparisons of nondimensional heat transfer rates from experiment[13] and the computational predictions given by LAURA. Note that the body-flap region was not computed for this comparison. Again, because the experiment contains natural transition from laminar to turbulent flow (denoted by the wedge-shaped rapid rise in heat transfer coefficient), both fully laminar and fully turbulent LAURA results are shown. For the laminar forebody region the heat-transfer patterns are very similar. However, upon comparing the after-body turbulent flow regions, it is apparent that the details of bow/wing-shock interaction are significantly smeared by the computation although the overall levels are comparable. Further comparison with experimental data is available in Refs. 13 and 45.

Surface Temperatures

This section presents the surface temperatures for all turbulent boundary-layer cases computed: cases 1a, 1b, 2a, and 2b. Discussion includes the effects of angle-of-attack variation and control-surface deflections.

Case 1a. Figure 13 shows surface-temperature contours for case 1a. Note that there are three contour-level legends, one for each of the lee-side, starboard, and wind-side views; these same three contour-level distributions are held constant for all subsequent

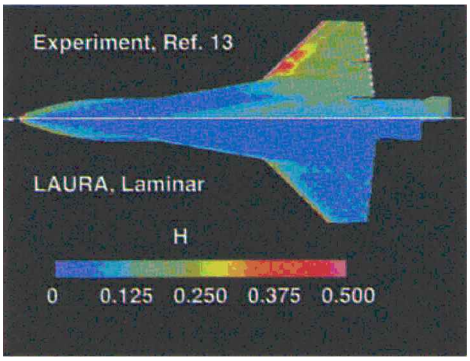

a) Laminar LAURA solution

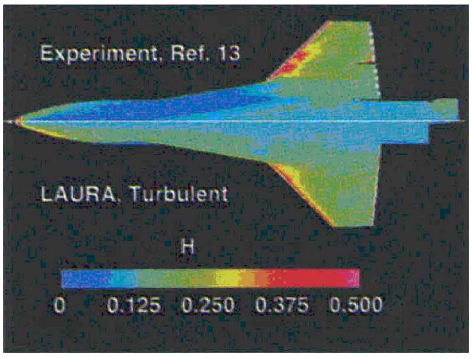

b) Turbulent LAURA solution

Fig. 12 A comparison of wind-side heat transfer between those measured by the phosphor thermography technique[45] and those computed by LAURA for wind-tunnel conditions (Mach 6, α = 15 deg, Re_L = 8×10^6, and δ_{cs} = 0 deg).

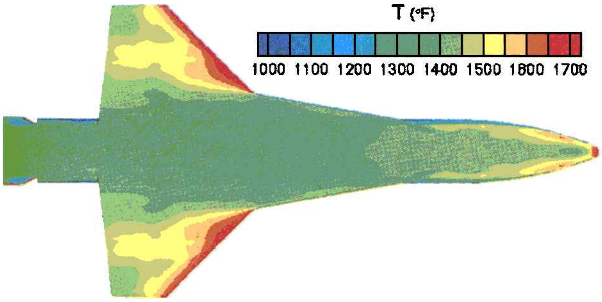

a) Wind side

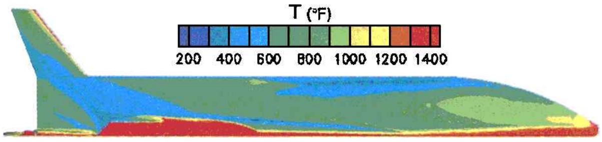

b) Starboard side

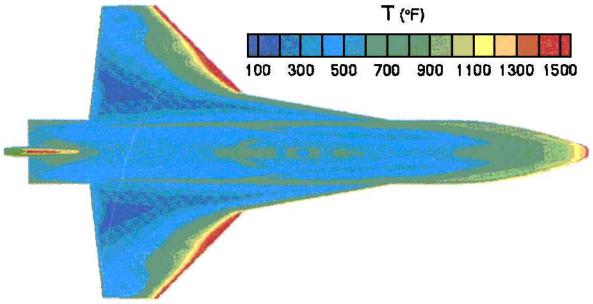

c) Lee side

Fig. 13 Surface temperatures (case 1a).

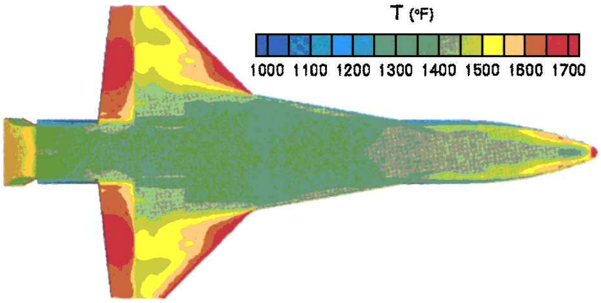

a) Wind side

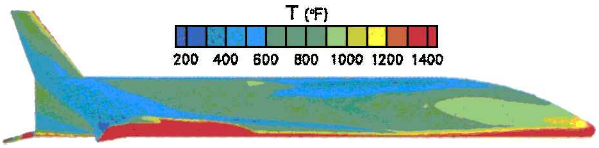

b) Starboard side

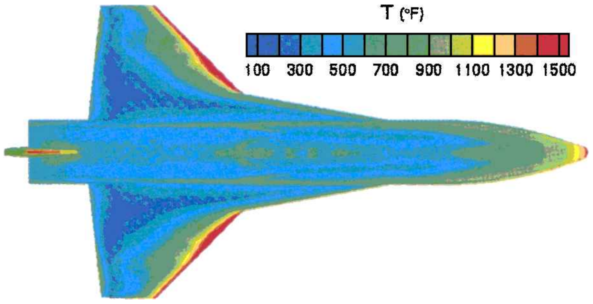

c) Lee side

Fig. 14 Surface temperatures (case 1b).

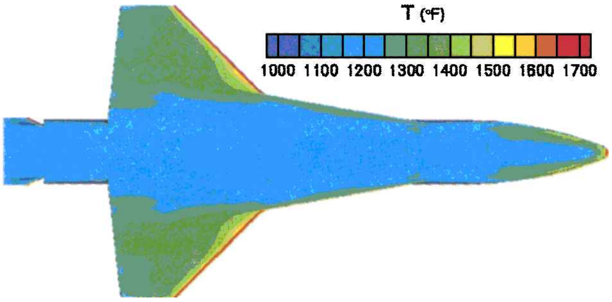

a) Wind side

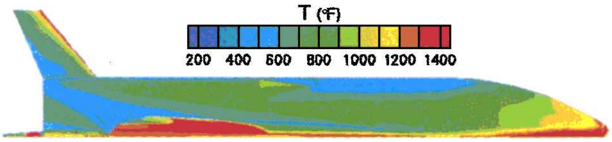

b) Starboard side

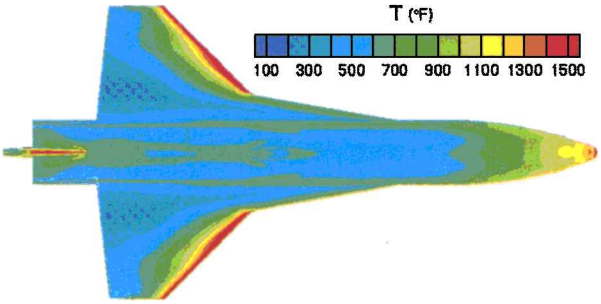

c) Lee side

Fig. 15 Surface temperatures (case 2a).

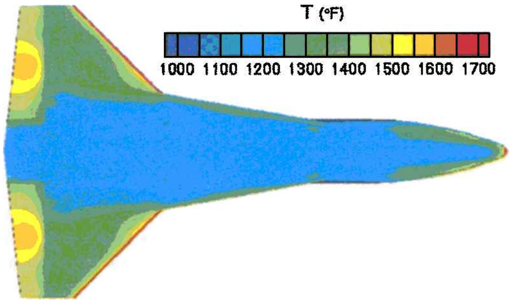

a) Wind side

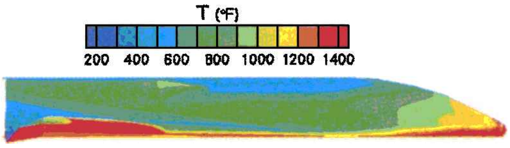

b) Starboard side

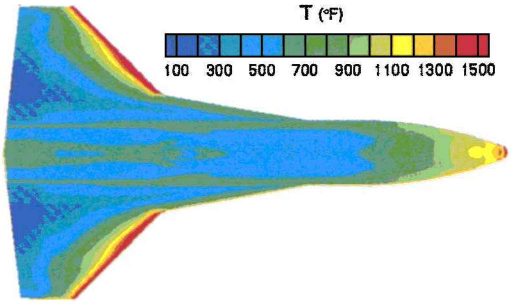

c) Lee side

Fig. 16 Surface temperatures (case 2b).

surface-temperature figures to facilitate comparison. The wind-side view shown in Fig. 13a shows the expected high temperatures for the nose stagnation region. The forebody chines also show significant temperature elevation due to the vehicle's forebody geometry approaching the bow shock generated by the spherical nose cap. Also present on Fig. 13a are streaks of elevated temperatures crossing the wings chord-wise. These streaks correspond to the remnants of the forebody bow shock (cf. Fig. 4a). Also, although not readily discernible with this choice of temperature contour levels, there is a second streak emanating from the bow/wing-shock interaction point just outside of the wing/strake juncture, raked aft from the leading edge of the wing. This second streak is readily apparent in the experimental results of Ref. 13. The vast acreage of the wind-side fuselage surface is in the range of 1300–1400°F.

Note that the outside edges of the body flap have slightly cooler temperatures than the inboard portion. This area of cooler temperatures is associated with near-surface streamlines that emanate from the leading edge of the notched body flap. This trend is erroneous as discussed earlier.

The starboard and lee-side views (Figs. 13b and 13c) show the effects of several flow features previously discussed. For instance, between the canopy and the round-to-squared fuselage transition, longitudinal low-temperature streaks are well defined, corresponding to the pair of vortices located just above the fuselage. As mentioned earlier, when the fuselage cross-section transition is encountered, an embedded shock is generated, which is indicated by the triangular-shaped region of higher temperatures in this area.

Case 1b. Surface temperatures for the deflected control surface, case 1b, are shown in Fig. 14. As compared to the undeflected case, the temperatures on the forebody are not affected by the change because the shock layer has supersonic flow. In fact, after verifying the lack of upstream influence, downstream configuration perturbations were accommodated by splitting the domain and using a cross-flow plane of data as an inflow condition for downstream blocks. As shown by Fig. 14a, the deflected surfaces now experience 200–300°F higher temperatures on their wind sides.

For this case, the nonphysical effect of having to run the notched body-flap region with the laminar equations is more readily apparent than for the undeflected case because the embedded body-flap-notch leading-edge shock (refer to Fig. 8) is stronger.

Although difficult to see in Figs. 13b and 14b, the wing wake is slightly larger for the deflected case. Also, the footprint of the wing fish-tail shock is at a lower angle relative to the vehicle's longitudinal axis.

Case 2a. Surface temperatures for this lower angle-of-attack case are shown in Fig. 15. As compared with case 1, the wind-side temperatures are on the order of 250°F lower while maintaining the same qualitative distribution, except for the wing-shock/bow-shock interaction occurring slightly closer to the fuselage. Figures 15c and 15b, however, show increased heating on the lee side. Most notable are the nose region and the tail leading edge. The fuselage transition area is also slightly hotter. The wing-wake structure appears to have higher energy as its temperature footprints are on the order of a 100°F higher than the higher angle-of-attack case. The terminating fish-tail shock appears at a more oblique angle.

Case 2b. The effects of deflecting the elevon control surface 10° are shown in Fig. 16. As for cases 1a and 1b, the forward portion of the vehicle is not affected by this change due to supersonic flow, and the deflection simply results in higher wind-side temperatures for the flap (see Fig. 16a). However, for this lower angle-of-attack case, there is a small area of flow separation near the outboard end of the elevon, resulting in slightly lower temperatures in this area. This is faintly visible in Fig. 16a as a sliver of blue along the hinge line between 70 and 80% span.

Heating Rates

Figures 13–16 have been presented in terms of temperatures because this is the most important quantity to consider when ensuring that TPS temperature limits are not violated. Estimates of the corresponding heating rates can be derived from the temperature distributions with Eq. (1) using the appropriate emissivity. An example of the heating-rate distribution is shown in Fig. 17 for case 2b.

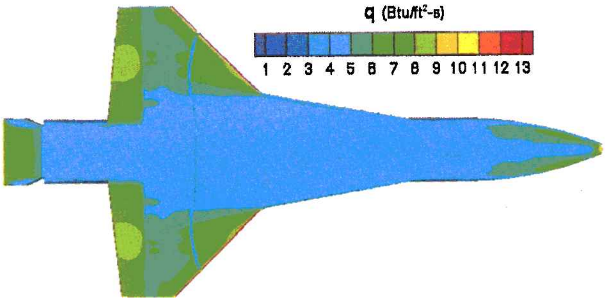

a) Wind side

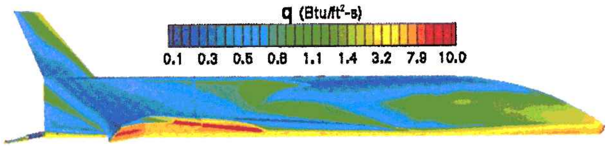

b) Starboard side

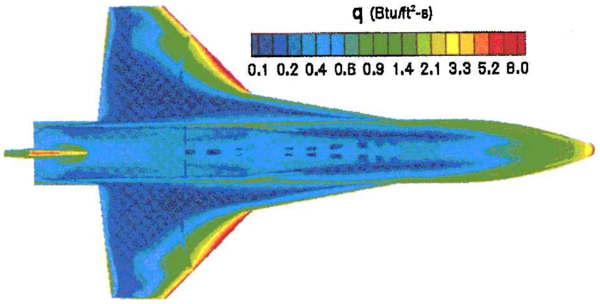

c) Lee side

Fig. 17 Heating rates (case 1b), turbulent.

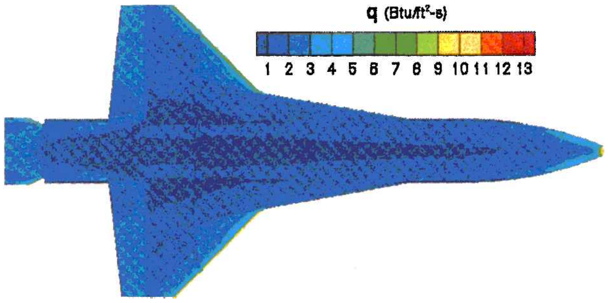

a) Wind side

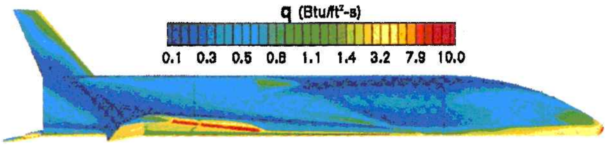

b) Starboard side

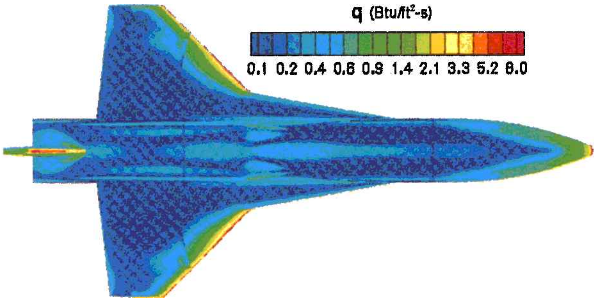

c) Lee side

Fig. 18 Heating rates (case 1b), laminar.

The dashed pattern of very low heating rates apparent on the lee side of the fuselage (see Fig. 17c) is because of an instability of the Baldwin–Lomax turbulence model when coupled with the iterative, radiative-equilibrium wall boundary condition in a multiple-block context. An improved algorithm for determining the location of the maximum vorticity within the boundary layer eliminated this problem in subsequent runs. This particular case was not recomputed because of limited resources and the fact that most regions of interest are outside the domain of dependence. The heating-rate distributions for the remaining cases are presented in Ref. 46.

Boundary-Layer State

For cases 1a and 1b, both laminar and turbulent boundary-layer solutions were obtained. This section provides a brief synopsis of the effects of the boundary-layer state, focusing on the deflected control surfaces of case 1b.

Figures 17 and 18 show surface heating rates for turbulent and laminar boundary layers, respectively. When Figs. 17 and 18 are compared, it is apparent that the turbulent boundary-layer assumption provides a more conservative estimate of the heating rates than the laminar boundary layer. Overall, the laminar heating rates tend to be half of those for the turbulent boundary layer. However, as is also evident if pressure distributions are examined, the qualitative agreement is very close, signifying that most of the heating patterns are determined by inviscid flow features such as shocks and vortex cores.

TPS Considerations

The first question of the proposed TPS design is whether multiple-use temperature limits will be exceeded in any area. To address this question, Fig. 19 shows the temperature distribution of the wind-side peak heating flight case 1b with deflected control surfaces overlaid on the TPS material schematic in terms of previously predicted temperature levels. In a small area, where the bow-shock interaction impinges the deflected elevon, the maximum temperature for the high heat blanket (HHB) is exceeded. However, the temperature excursion is not large, and the vehicle is anticipated to fly this portion of the trajectory with undeflected or upwardly deflected elevons. The lee side is examined using the temperature distributions from case 2a since it was shown earlier to have a more extreme lee-side environment even though it is slightly after peak nose heating in the flight trajectory. This overlay is shown in Fig. 20. As a result of these data, the bond line between the LHB and FRSI blankets on the lee side near the wing leading edge was moved aft to account for the increased exposure found at 15-deg angle of attack. In addition, the TPS split line on the lee side of the nose region was also moved aft.

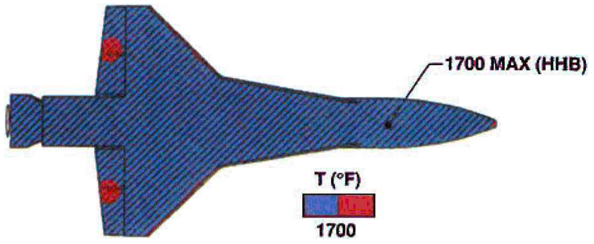

Fig. 19 Wind-side TPS layout and temperature limits overlaid with computed temperature contours (case 1b).

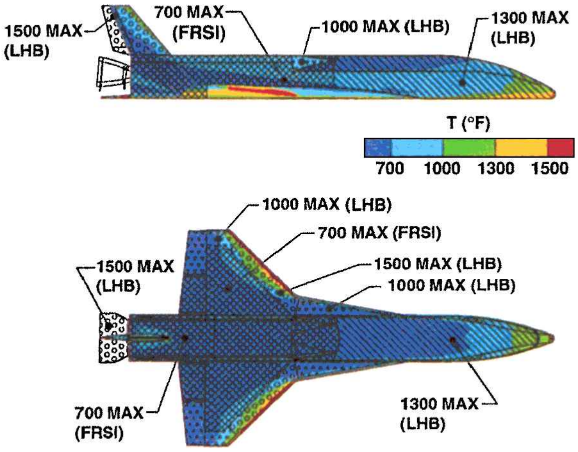

Fig. 20 Lee-side TPS layout and temperature limits overlaid with computed temperature contours (case 2a).

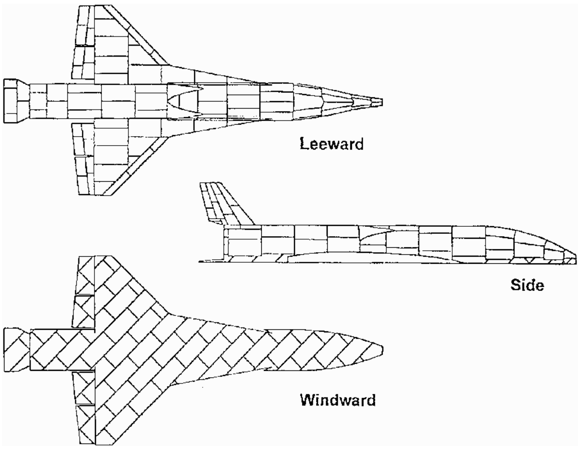

Fig. 21 Thermal protection blanket layout.

By comparing the predicted near-surface streamlines of Figs. 9 and the TPS blanket orientations shown in Fig. 21, one can investigate aspects of the TPS orientations. For example, upon carefully examining these figures, it is evident that no blanket-to-blanket or blanket-to-tile gaps are aligned with the local flow for these flight conditions.

Concluding Remarks

Radiative-equilibrium surface temperatures, heating rates, streamlines, surface pressures, and flowfield features as predicted by LAURA were presented for the X-34 Technology Demonstrator. Results for two trajectory points near peak heating and the effects of control-surface deflections were presented for fully turbulent flow. Laminar flow results that illustrate the effects of the boundary-layer state also were presented. The effects of the results on the TPS design also were indicated.

Results show that downward deflection of control surfaces substantially increases the temperatures they experience during flight. Furthermore, a notched body-flap design creates an embedded shock, which creates large local heating rates on the tapered portion of the body-flap side wall. The effect of lowering the angle of attack from 23 to 15 deg at flight conditions was shown to substantially increase the extent of lee-side heating on the nose-canopy region and aft of the wing leading edges. Also shown was that if the boundary layer was modeled as purely laminar, the predicted wind-side surface temperatures would be 500–600°F lower than that obtained if a fully turbulent boundary layer was modeled.

Acknowledgments

We would like to thank Orbital Sciences Corporation of Dulles, Virginia, for providing the impetus for such an exciting project. The authors would like to thank Graphic Artist Richard Wheless of NCI Information Systems, Hampton, Virginia, for generating Fig. 1, Norma Bean of Computer Sciences Corporation, Hampton, Virginia, for generating the surface grid database, and Ronald Merski of NASA Langley Research Center, Hampton, Virginia, for providing the additional off-centerline data used to produce Fig. 11b.

References

[1] Elias, A. L., Hays, D., and Kennedy, J., "Pioneering Industry/Goverment Partnerships: X-34," AIAA Paper 95-3777, Sept. 1995.

[2] "X-34 to be Acid Test for Space Commerce," *Aviation Week and Space Technology*, Vol. 142, No. 14, 1995, pp. 44–53.

[3] "Reusable Launch Vehicle (RLV), Small Reusable Booter, X-34," NASA Cooperative Agreement Notice CAN 8-2, Jan. 1995.

[4] Freeman, D. C., Jr., Talay, T. A., and Austin, R. E., "Single-Stage-to-Orbit—Meeting the Challenge," *Acta Astronautica*, Vol. 38, No. 4–8, 1996, pp. 323–331.

[5] Smith, B. A., and Asker, J. R., "NASA Speeds Selection of X-33, X-34 Plans," *Aviation Week and Space Technology*, Vol. 142, No. 11, 1995, pp. 107–109.

[6] Foley, T. M., "Big Hopes for Small Launchers, " *Aerospace America*, Vol. 33, No. 7, 1995, pp. 28–34.

[7] "X-34 in Virtual Shutdown as OSC Ponders Pullout," *Aviation Week and Space Technology*, Vol. 144, No. 6, 1996, p. 86.

[8] Anselmo, J. C., "NASA Issues Wake-Up Call to Industry," *Aviation Week and Space Technology*, Vol. 144, No. 8, 1996, pp. 20, 21.

[9] *Proceedings of the X-15 First Flight 30th Anniversary Celebration*, NASA CP-3105, June 1991.

[10] Eisele, A., "Orbital Sciences Gets X-34 Nod Again," *Space News*, Vol. 7, No. 25, 1996, p. 4.

[11] Anselmo, J. C., "NASA Gives Second Shot at X-34," *Aviation Week and Space Technology*, Vol. 144, No. 25, 1996, p. 31.

[12] Riley, C. J., Kleb, W. L., and Alter, S. J., "Aeroheating Predictions for X-34 Using an Inviscid Boundary-Layer Method," *Journal of Spacecraft and Rockets*, Vol. 36, No. 2, 1999, pp. 206–215.

[13] Berry, S. A., Horvath, T. J., DiFulvio, M., Glass, C. E., and Merski, N. R., "X-34 Experimental Aeroheating at Mach 6 and 10," *Journal of Spacecraft and Rockets*, Vol. 36, No. 2, 1999, pp. 171–178.

[14] Wurster, K. E., Riley, C. J., and Zoby, E. V., "Engineering Aerothermal Analysis for X-34 Thermal Protection Design," *Journal of Spacecraft and Rockets*, Vol. 36, No. 2, 1999, pp. 216–228.

[15] Palmer, G., and Polsky, S., "Heating Analysis of the Nosecap and Leading Edges of the X-34 Vehicle," *Journal of Spacecraft and Rockets*, Vol. 36, No. 2, 1999, pp. 199–205.

[16] Milos, F. S., and Squire, T. H., "Thermostructural Analysis of X-34 Wing Leading-Edge Tile Thermal Protection System," *Journal of Spacecraft and Rockets*, Vol. 36, No. 2, 1999, pp. 189–198.

[17] Gnoffo, P. A., "Upwind-Biased, Point-Implicit Relaxation Strategies for Viscous, Hypersonic Flows," AIAA Paper 89-1972, June 1989.

[18] Gnoffo, P. A., "An Upwind-Biased, Point-Implicit Relaxation Algorithm for Viscous, Compressible Perfect-Gas Flows," NASA TP-2953, Feb. 1990.

[19] Gnoffo, P. A., Gupta, R. N., and Shinn, J., "Conservation Equations and Physical Models for Hypersonic Air Flows in Thermal and Chemical Nonequilibrium," NASA TP-2867, 1989.

[20] Roe, P. L., "Approximate Riemann Solvers, Parameter Vectors, and Difference Schemes," *Journal of Computational Physics*, Vol. 43, No. 2, 1981, pp. 357–372.

[21] Harten, A., "High Resolution Schemes for Hyperbolic Conservation Laws," *Journal of Computational Physics*, Vol. 49, No. 2, 1983, pp. 357–393.

[22] Yee, H. C., "On Symmetric and Upwind TVD Schemes," NASA TM-88325, 1986.

[23] Mitcheltree, R. A., "Computational Aerothermodynamics for Mars Pathfinder Including Turbulence," AIAA Paper 95-3493, Aug. 1995.

[24] Gnoffo, P. A., Weilmuenster, K. J., Braun, R. D., and Cruz, C. I., "Effects of Sonic Line Transition on Aerothermodynamics of the Mars Pathfinder Probe," AIAA Paper 95-1825, June 1995.

[25] Mitcheltree, R. A., Moss, J. N., Cheatwood, F. M., Greene, F. A., and Braun, R. D., "Aerodynamics of the Mars Microprobe Entry Vehicles," AIAA Paper 97-3658, Aug. 1997.

[26] Mitcheltree, R. A., Wilmoth, R. G., Cheatwood, F. M., Brauckmann, G. J., and Greene, F. A., "Aerodynamics of Stardust Sample Return Capsule," AIAA Paper 97-2304, June 1997.

[27] Wood, W. A., Gnoffo, P. A., and Rault, D. F. G., "Aerodynamic Analysis of Commercial Experiment Transporter Re-Entry Capsule," *Journal of Spacecraft and Rockets*, Vol. 33, No. 5, 1996, pp. 643–646.

[28] Hamilton, H. H., II, Weilmuenster, K. J., and Horvath, T. J., "Computational/Experimental Aeroheating Predictions for X-33 Phase II Vehicle," AIAA Paper 98-0869, Jan. 1998.

[29] Greene, F. A., Weilmuenster, K. J., and Micol, J. R., "Predicted Aerodynamics for a Proposed Personnel Launch Vehicle," AIAA Paper 90-1668, June 1990.

[30] Kleb, W. L., and Weilmuenster, K. J., "Characteristics of the Shuttle Orbiter Leeside Flow During a Re-Entry Condition," *Journal of Spacecraft and Rockets*, Vol. 31, No. 1, 1994, pp. 8–16; also AIAA Paper 92-2951, July 1992.

[31] Weilmuenster, K. J., Gnoffo, P. A., and Greene, F. A., "Navier–Stokes Simulations of the Shuttle Orbiter Aerodynamic Characteristics with Emphasis on Pitch Trim and Bodyflap," AIAA Paper 93-2814, July 1993.

[32] Gnoffo, P. A., Weilmuenster, K. J., and Alter, S. J., "Multiblock Analysis for Shuttle Orbiter Re-Entry Heating from Mach 24 to Mach 12," *Journal of Spacecraft and Rockets*, Vol. 31, No. 3, 1994, pp. 367–377.

[33] Wood, W. A., Riley, C. J., and Cheatwood, F. M., "Reentry-F Flowfield Solutions at 80,000 ft," NASA TM-112856, May 1997.

[34] Baldwin, B. S., and Lomax, H., "Thin Layer Approximation and Algebraic Model for Separated Turbulent Flows," AIAA Paper 78-257, Jan. 1978.

[35] Gupta, R. N., Lee, K. P., Zoby, E. V., Moss, J. N., and Thompson, R. A., "Hypersonic Viscous Shock-Layer Solutions over Long Slender Bodies—Part I: High Reynolds Number Flows," *Journal of Spacecraft and Rockets*, Vol. 27, No. 2, 1990, pp. 175–184.

[36] Cheatwood, F. M., and Thompson, R. A., "The Addition of Algebraic Turbulence Modeling to Program LAURA," NASA TM-107758, April 1993.

[37] Spalart, P. R., and Allmaras, S. R., "A One-Equation Turbulence Model for Aerodynamic Flows," AIAA Paper 92-0439, Jan. 1992.

[38] Smith, B., Rinaudot, G. R., Reed, K. J., and Wright, T., "Initial Graphics Exchange Specification (IGES): Version 4.0," NBSIR 88-3813, June 1988.

[39] Akdag, V., and Wulf, A., "Integrated Geometry and Grid Generation System for Complex Configurations," NASA CP-3143, April 1993.

[40] Samareh-Abolhassani, J., "GridTool: A Surface Modeling and Grid Generation Tool," *Proceedings of the Workshop on Surface Modeling, Grid Generation, and Related Issues in CFD Solutions*, edited by R. E. Smith, NASA CP-3291, 1995, pp. 821–831.

[41] Steinbrenner, J. P., Chawner, J. R., and Fouts, C. L., "The GRIDGEN 3D Multiple Block Grid Generation System," Wright Research and Development Center, Rept. WRDC-TR-90-3022, Wright–Patterson AFB, OH, Oct. 1989.

[42] Alter, S. J., and Weilmuenster, K. J., "The Three-Dimensional Multi-Block Advanced Grid Generation System (3DMAGGS)," NASA TM-108985, April 1993.

[43] Alter, S. J., "The Volume Grid Manipulator (VGM): A Grid Reusability Tool," NASA CR-4772, April 1997.

[44] Alter, S. J., "Surface Modeling and Grid Generation of Orbital Sciences X34 Vehicle (Phase I)," NASA CR-97-206243, Nov. 1997.

[45] Merski, N. R., "Global Aeroheating Wind-Tunnel Measurements Using Improved Two-Color Phosphor Thermography Method," *Journal of Spacecraft and Rockets*, Vol. 36, No. 2, 1999, pp. 160–170.

[46] Kleb, W. L., Wood, W. A., and Gnoffo, P. A., "Computational Aeroheating Predictions for X-34," NASA TM-1998-206289, Jan. 1998.

[47] Wood, W. A., "Aerothermodynamic Calculations on X-34 at Mach 6 Wind Tunnel Conditions," NASA TM-1999-208998, Feb. 1999.

T. C. Lin
Associate Editor

Color reproductions courtesy of NASA Langley Research Center